New M_3O_5-Anatase Intergrowth Structures Formed during Low-Temperature Oxidation of Anosovite

I. E. Grey,* L. M. D. Cranswick,† C. Li,* T. J. White,‡ and L. A. Bursill§

*CSIRO Minerals, Clayton, Victoria 3168, Australia; †CLRC Daresbury Laboratory, Warrington, WA4 4AD, United Kingdom; ‡Environmental Technology Institute, Singapore 639798, Singapore; and §School of Physics, University of Melbourne, Parkville 3052, Australia

Oxidation of anosovite at temperatures $\leq 300°C$ produces new phases of general composition M_nO_{2n-1}, based on unit cell intergrowth of M_3O_5 and anatase structural elements. The structural principles on which the intergrowth series are based were established by analysis of high-resolution transmission electron microscope images. The structure for the dominant intergrowth phase, with composition M_6O_{11}, was refined using the Rietveld method applied to powder X-ray data. This phase has monoclinic symmetry and space group $C2/m$, with $a = 9.946(2)$, $b = 3.744(2)$, $c = 20.994(3)$ Å, and $\beta = 93.30(1)°$. Its structure comprises planar intergrowth of M_3O_5 compositional blocks with the pseudobrookite-type structure and MO_2 compositional blocks with the anatase-type structure, parallel to $(001) \equiv (001)_{M_3O_5} \equiv (101)_{an}$. Alternatively, the structure can be considered as chemically twinned anatase with $(101)_{an}$ as the twin composition plane. The anatase blocks are alternately 2-octahedra and 3-octahedra wide along [001]. Local regions corresponding to compositions M_5O_9 (twinned anatase blocks are 2-octahedra wide) and M_7O_{13} (3-octahedra wide anatase blocks) were also observed in TEM images. The results have relevance to the digestion of high-titania slags (anosovite-rich) in the sulfate-route titania pigment process because high sulfuric acid solubility is maintained after the low-temperature treatment, while the preoxidation of trivalent titanium avoids acid consumption by solution oxidation. © 2000 Academic Press

INTRODUCTION

Titanium dioxide, by virtue of its high refractive index and nontoxicity, has important, high-volume applications in paints, paper, plastics, and ceramics. Half of the +3 million tpa of titania pigment is prepared by the sulfate process (1), whereby titania-bearing feedstocks are digested in concentrated sulfuric acid and high-purity titania is recovered by hydrolysis. Ilmenite, $FeTiO_3$, has been the traditional feedstock, but environmental problems associated with the disposal of ferrous sulfate have led to the consideration of alternative, higher titania feedstocks. These include high-titania slags produced by smelting of ilmenite (2) as well as acid-soluble products from ilmenite upgrading at subslagging temperatures (3). In both cases the dominant constituent which confers acid solubility is a phase of composition M_3O_5. More specifically, this can be expressed as a solid solution of the type $(M^{2+}Ti_2O_5)_x(M_2^{3+}TiO_5)_{1-x}$, where $M^{2+} = $ Mg, Mn, Fe and $M^{3+} = $ Ti, Al. These phases have the pseudobrookite structure or a monoclinic distortion of it for $x < 0.3$ (4). Ti_3O_5-rich M_3O_5 compositions are known as anosovite (5).

Anosovite-rich feedstocks are desirable to minimize metal sulfate effluents, but the high-trivalent titanium content can result in acid consumption by the oxidation reaction, $Ti_3O_5 + H_2SO_4 \rightarrow 3TiO_2 + H_2O + SO_2$ (6), as part of a general study on sulfate-route feedstocks (4, 6–8), we investigated the potential of low-temperature oxidation of anosovite for removing trivalent titanium while still maintaining the high acid solubility characteristics. Powder X-ray diffraction (PXRD) and electron diffraction (ED) studies of products from heating anosovite in air at temperatures below 300°C showed the formation of a new phase in which two of the axes of the anosovite unit cell were maintained and a superstructure had developed along the third direction. High-resolution transmission electron microscope (TEM) images were used to construct a model for the new phase, based on ordered intergrowth of M_3O_5 and anatase structure components. The structure was refined using the Rietveld method applied to the PXRD data. The ED and high-resolution electron microscopy (HREM) studies showed that considerable microtwinning and disorder existed in the low-temperature oxidation products and that locally a variety of different superstructures formed in local regions of the samples. The structural variations were interpreted within the context of anatase–anosovite intergrowths. One of these variants has recently been reported as an extended defect, found in a TEM study of samples produced by the reduction of $(V, Ti)O_{2-x}$ in argon at 1600°C (9).

We report here the results of PXRD and TEM studies on products obtained from low-temperature treatment of anosovite samples.

EXPERIMENTAL

Anosovite Preparations

A synthetic anosovite-type M_3O_5 phase, with composition $Mg_{0.3}Ti_{2.7}O_5$, was prepared by reduction of the appropriate mixture of MgO (from calcined AR $MgCO_3$) and TiO_2 in a H_2/CO_2 gas mixture at 1200°C. The gas composition was adjusted to give an oxygen fugacity of $10^{-15.6}$ atm, which is within the stability field for single-phase M_3O_5 in the Mg–Ti–O system (4). Anosovite samples were also prepared by reduction of natural ilmenite with char or H_2/CO_2 gas mixtures under conditions where the majority of the iron in the ilmenite was converted to the metal. Under these conditions natural ilmenites, with moderate (3–5 wt%) levels of MgO + MnO impurities give reduction products comprising $Fe^0 + M_3O_5$. For ilmenite samples with low impurity levels it is necessary to add MgO and/or MnO to fully stabilize the M_3O_5 phase (3); otherwise, the product will contain reduced rutile phases, Ti_nO_{2n-1} (10). The reduced ilmenite (RI) samples were leached in dilute H_2SO_4 at 60°C to remove the metallic iron and give an anosovite product (6).

Phase Characterization

Elemental analyses of anosovite samples and their oxidation products were made using X-ray fluorescence spectroscopy on fused discs. Analyses for trivalent titanium were made by both redox titration (after dissolution in H_2SO_4/HF containing excess V^{5+}) and by quantitative oxidation to TiO_2 at 900°C. Results obtained by the two procedures were in good agreement.

PXRD was used for the routine identification of phases in the equilibrated products and to provide intensity data for structure refinements by the Rietveld method (11). Samples for PXRD were prepared by grinding and back-pressing the powders into an aluminum sample holder. Measurements of diffracted intensities were made using a Philips 1050 goniometer with a PW1710 controller and using a long fine-focus copper tube operated at 40 kV and 40 mA. The diffractometer was configured with a 1° divergent slit, 0.2-mm receiving slit, 1° scatter slit, incident and diffracted beam Soller slits, and a diffracted-beam curved graphite monochromator. Step-scan intensity measurements in the 2θ range 10°–120° were made at intervals of 0.025°, with a step-counting time of 12 s.

Least-squares refinements of the structural model were initially carried out using the Rietveld program SR5, a local modification of the code by Hill and Howard (12) and Wiles and Young (13) which allows for quantitative phase analysis of multi-phase mixtures. Profile refinement parameters included a scale factor, two pseudo-Voigt shape parameters, a 2θ zero parameter, a three-term full-width at half-maximum function (14), calculated for 11 half-widths on either side of the peak maxima, a peak asymmetry parameter for peaks less than 50° 2θ, and unit cell parameters. The background was modeled using a four-parameter polynomial fit. Scattering curves for ionized atoms were taken from "International Tables for X-ray Crystallography" (15).

It was found that due to disorder in the samples and peak broadening, the quality of the data sets was not adequate for unrestrained refinement of the oxygen positions. A change was thus made to the Fundamental Parameters Rietveld program Topas (16) in which bond restraints and anti-bump criteria on O–O, M–M, and O–M could be defined by macros and suitable weighting schemes for the restraints were established in the refinement process.

Electron diffraction/microscopy studies were made using a JEOL 4010 transmission electron microscope operated at 400 keV. Studies were made on thin edges of crystals produced by fracturing. Images were collected near the Scherzer defocus condition. Image simulations were calculated using a multislice image calculation program developed at Melbourne University Physics Department (17). Calculations were made for a microscope resolution of 2.5 Å, for defocus values close to the Scherzer condition, from −350 to −550 Å, and for crystal thicknesses in the range 20–100 Å.

RESULTS AND DISCUSSION

Low-Temperature Oxidation of Anosovite

Trivalent titanium analyses and calculated percentage oxidations for the products from selected air oxidation runs on $Mg_{0.3}Ti_{2.7}O_5$ at different temperatures and times are given in Table 1. The phase changes accompanying oxidation were monitored using PXRD and the phases found are given in Table 1. For the oxidation times where residual anosovite was present in the product, the oxidation kinetics followed at $t^{1/2}$ dependence, indicative of a diffusion-controlled process. From an Arrhenius plot of the rate data in the temperature range 200–300°C an activation energy of 12 kcal/mol was derived. Beyond the time where anosovite could no longer be distinguished in the PXRD patterns the oxidation rate decreased markedly, even though only ~50% of the oxidation had occurred.

An oxidation test was also conducted on synthetic anosovite in refluxing 5% (w/w) H_2SO_4. The sample underwent a 5.7% weight loss after 10 h of treatment. An analysis for trivalent titanium in the product showed that 28% oxidation had occurred. The PXRD pattern for the product was almost identical to that for the sample heated in air at 200°C to the same degree of oxidation (see Table 1).

GREY ET AL.

TABLE 1
Results from Selected Oxidation Experiments on $Mg_{0.3}Ti_{2.7}O_5$

Oxidation temp., °C	Oxidation time, min	wt% Ti^{3+}	% oxidation	Phases form XRD
25		30.2	None	Starting phase, M_3O_5
200	30	26.2	13	M_3O_5 + phase A (trace)
	120	21.7	28	M_3O_5 (major) + phase A (minor)
	360	13.8	54	M_3O_5 (minor) + phase A (major)
250	30	14.9	51	M_3O_5 (minor) + phase A (major)
	120	10.9	64	Phase A
	480	9.2	69	Phase A
300	30	5.5	82	Phase A
400	30	1.8	94	Phase B
600	30	0	100	Phase B
	48 h	0	100	Phase B + rutile (trace)
700	30	0	100	As above
800	30	0	100	Anatase (major) + rutile (minor) + $MgTiO_3$ (trace) + $MgTi_2O_5$ (trace)
900	16 h	0	100	Rutile (major) + $MgTi_2O_5$ (minor) + anatase (trace)

PXRD patterns of the starting anosovite phase and products after different oxidation treatments are illustrated in Fig. 1. Pattern (b) is from a sample obtained by heating $Mg_{0.3}Ti_{2.7}O_5$ for 30 min at 300°C (= phase A in Table 1). It differs markedly from the pattern of the starting anosovite, Fig. 1a, through the disappearance and/or shifting of a number of peaks and the appearance of many new peaks which are considerably broadened relative to those in the anosovite pattern. Similar patterns were obtained for all samples oxidized at or below 300°C, where the degree of oxidation was of the order of 60% or higher. For example, anosovite samples which were prepared by reducing ilmenite and leaching the metallic iron in 5% H_2SO_4 and were then heated in air at 110°C for 12 months, gave almost identical PXRD patterns in that in Fig. 1b.

Significant changes in the PXRD patterns were observed when the oxidation temperature was increased to 400°C, as shown in Fig. 1c (= phase B in Table 1). A number of peaks disappeared and others broadened, decreased in height, and shifted in position. These changes continued when the temperature was increased to 500 and 600°C. With increasing temperature and oxidation time, the PXRD patterns progressively adopted the general features of the anatase pattern, although there were some major differences with regard to the positions and relative intensities of the group of reflections in the 2θ range 36°–39°, as seen by a comparison with the pattern for pure anatase in Fig. 1d. After prolonged heating at 600°C, the PXRD patterns showed the initiation of the anatase to rutile transformation. At 900°C the main products were rutile and M_3O_5, with a trace of residual anatase.

A striking feature of all the patterns in Fig. 1 is the presence of strong reflections at d spacings of 3.51 and 1.87 Å ($2\theta = 25.4°$ and 48.5°). The planes giving rise to these reflections in anatase and anosovite are illustrated in Fig. 2. It is seen from Fig. 2 that there is a close topological relationship between anosovite and anatase in the projections shown (only the $M(2)O_6$ octahedra are shown for anosovite to emphasize this relationship). Note that the plane indexing given in Fig. 2 (and elsewhere in this paper) for the M_3O_5 phase is based on the space group $Ccmm$, consistent with our previous studies (4). On this basis, the unit cell parameters of $Mg_{0.3}Ti_{2.7}O_5$ are $a = 9.807$, $b = 3.780$, and $c = 9.977$ Å. The cell parameters for anatase, with space group $I4_1/amd$, are $a = 3.784$ and $c = 9.514$ Å (18).

The retention of the dominant diffraction features at d spacings of 3.51 and 1.87 Å in the intermediate oxidation products constrains the structural modifications that are possible as a result of the oxidation. In particular, it indicates that a 3.8 Å axis ($\equiv$ periodicity of corner-linked octahedra) is maintained. However, even with this information, an unambiguous indexing of the powder pattern was not possible, due largely to overlapping reflections that were unresolved because of the broadness of the peaks. This problem was overcome through the application of electron diffraction/microscopy.

TEM Studies

ED patterns obtained for phase A ($\leq 300°C$, Fig. 1b) oxidation product were indexed on the basis of a monoclinic

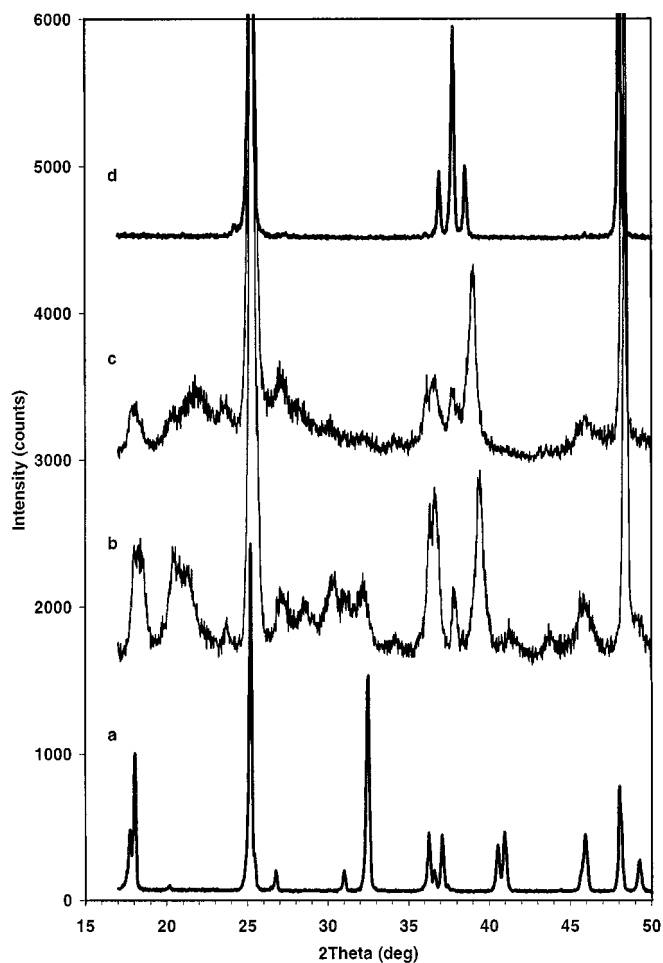**FIG. 1.** PXRD patterns for (a) $Mg_{0.3}Ti_{2.7}O_5$, (b) oxidation product from 30 min at 300°C, (c) oxidation product from 30 min at 400°C, and (d) anatase, CuKα radiation.

Changes in the periodicity normal to (001) planes were commonly observed in small regions of the images. An example is given in Fig. 4a. The left half of this image shows a c-axis periodicity of 24.9 Å ≡ //V\\Λ// ..., while the right half exhibits a c-axis periodicity of 17.3 Å ≡ /V\Λ/ ..., albeit only for two unit cells in each case. Figure 4b illustrates periodicity variations around a residual region of M_3O_5, shown by the sequence ΛVΛ in the lower central region of the diagram. There is a 21-Å c-axis periodicity on either side of the residual M_3O_5 but a local 17.3-Å periodicity above. The progressive structure modifications associated with the oxidation process are clearly seen around the edge of the M_3O_5 region.

A [010] zone axis ED pattern for a sample oxidized at 400°C (PXRD pattern in Fig. 1c) is presented in Fig. 5. The indexing shown is in relation to anatase, to which the phase is closely related. Diffuse streaking occurs parallel to $[101]^*_{an}$. The corresponding image shows complex structural intergrowths, with extended regions containing only the features ...///....

Structural Model for the ≤300°C Oxidation Product

A structural model for the ≤ 300°C oxidation product, phase A, was established from an interpretation of the high-resolution TEM images such as those shown in Fig. 3. The images were obtained at close to the Scherzer defocus condition, and an interpretation of the white features as projected low electron density regions gave a model which could be refined using the PXRD data and which was shown to be consistent with multislice image calculations.

The model was established by interpreting the V features as regions of M_3O_5 and the // features as anatase regions. The basis for this is shown in Fig. 6, where below the 3.8-Å projections of polyhedral models for M_3O_5 and anatase are shown the metals only, in the same 3.8-Å projections. The metal atoms, as the most strongly electron-scattering atoms, have been enlarged until they overlap. This accentuates the shape of the "holes" between the metals which are seen to be consistent with the VΛV features in M_3O_5 and /// in anatase. There is a close match of these features with the results of multislice image calculations for M_3O_5 and anatase, shown also in Fig. 6.

In Fig. 6, the anatase structure is shown with $[-101]_{an}$ direction vertical and thus parallel to $[100]_{M_3O_5}$. It is seen that there is a close structural match of the $(101)_{an}$ and $(001)_{M_3O_5}$ planes. A model for the ≤ 300°C oxidation product was constructed based on intergrowth of two-dimensional slabs of the two structure types, parallel to these planes and consistent with the unit cell geometry determined from the ED patterns. The centosymmetric space group, $C2/m$, was assumed. The model is shown in Fig. 7. Assuming full occupancy of the structural sites, the unit cell composition is $M_{24}O_{44} = 4 \times M_6O_{11}$. Based on the
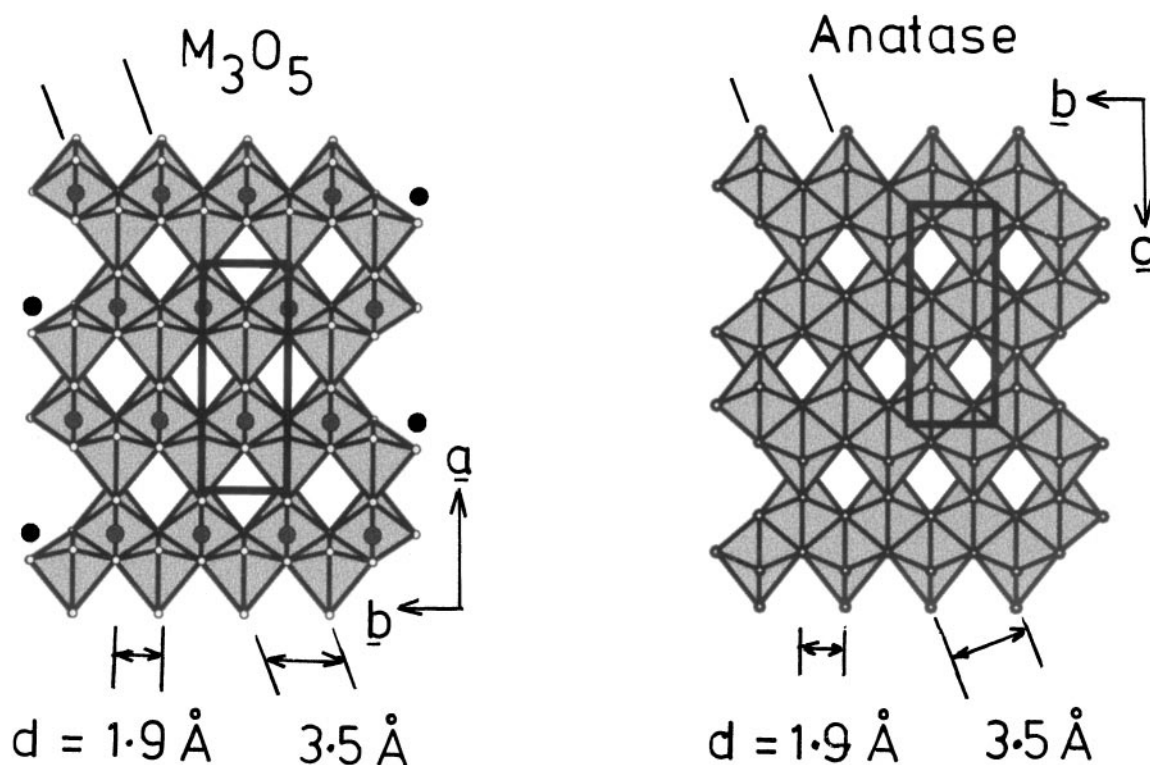
cell with $a = 9.94$, $b = 3.74$, $c = 21.0$ Å, and $\beta = 93°$. Systematic absences were consistent with possible space groups $C2/m$, Cm, and $C2$. A typical ED pattern, with [010] as the zone axis, is illustrated in Fig. 3. Characteristic features include strong diffuse scattering parallel to the c^* direction and spot doubling due to microtwinning. As a consequence of the cell shape, the twinning results in almost exact superposition of twin spots for ($h0l$) reflections with $h = 4n$ and shows an apparent halving of c^* for $h = 4n + 2$. A high-resolution image corresponding to the [010] zone axis DP is also shown in Fig. 3. Except right at the crystal edge (bottom right-hand side) the ~150 Å region covered by the image is homogeneous with a well-defined c-axis periodicity of 21 Å. The white motifs comprising the repeat unit along [001] in the image can be represented schematically in terms of two types of features (vees and slashes) as ...//V\Λ//.... These features are repeated in strings along [100] with a projected repeat distance of 5 Å = 0.5a.

FIG. 2. Polyhedral projections of the anatase structure along $[100]_{an}$ and the M_3O_5 structure along $[001]_{M_3O_5}$, showing common planes in the two structures with d spacings of 1.9 and 3.5 Å. In M_3O_5, only the octahedra around $M(2)$ are shown. $M(1)$ is represented by filled circles.

starting composition for the oxidation experiments, the charge-balanced composition is calculated from the structure model to be $Mg_{0.6}Ti_{0.8}^{3+}Ti_{4.6}^{4+}O_{11}$. The calculated Ti^{3+} content is 8.3 wt%.

For the two other intergrowth sequences shown in Fig. 4a, a similar treatment to the above allows the compositions to be calculated, giving $M_7O_{13} = Mg_{0.6}Ti_{0.8}^{3+}Ti_{5.6}^{4+}O_{13}$ for the 24.9-Å periodicity and $M_5O_9 = Mg_{0.6}Ti_{0.8}^{3+}Ti_{3.6}^{4+}O_9$ for the 17.3-Å periodicity. The calculated Ti^{3+} contents for these two phases are 5.5 and 12.9 wt%, respectively. These values span the experimental Ti^{3+} ranges obtained from analyses of $\leq 300°C$ oxidation products reported in Table 1. An intergrowth phase of M_5O_9 composition was reported recently as an extended defect, found in a TEM study of samples produced by the reduction of $(V, Ti)O_{2-x}$ in argon at 1600°C (9). The intergrowth composition corresponding to full oxidation of titanium is $M_{10}O_{19} = MgTi_9O_{19}$.

Rietveld Refinement of the M_6O_{11} Model

Starting coordinates for the Rietveld refinement were obtained directly from scale drawings of the intergrowth model, based on published parameters for $Mg_{0.6}Ti_{0.8}^{3+}$

$Ti_{4.6}^{4+}O_{11}$ (4) and anatase (18). It was apparent from the refinement that some weak peaks in the pattern were not being fitted by the unit cell for M_6O_{11}. Patterns were calculated for other intergrowths observed in the TEM images (Fig. 4a). These showed that the extra peaks corresponded to the M_5O_9 intergrowth. This was included as a second phase in the refinement. The ideal atomic coordinates obtained from a scale drawing for M_5O_9 were kept fixed in the refinement. Interatomic distance restraints and antibumping functions were used to keep the refinement as physically reasonable as possible, within the limitations of the relatively poor data and the complex structure. The strong peaks at $2\theta = 25.4°$ and $48.5°$ had calculated intensities significantly lower than the observed peaks. As seen from Fig. 1, these peaks are common to both anosovite and anatase as well as their intergrowths, suggesting that disordered intergrowth sequences are contributing to their intensities. The extra intensity for these two peaks was taken up by pseudo-voigt peaks during the refinement.

Group isotropic displacement parameters were used for the metal atoms and oxygens. These were initially refined and then fixed at values of 0.25 and 0.6 $Å^2$, respectively. No attempt was made to model the small amount of Mg in the metal atom sites. The scattering curve for titanium (as Ti^{4+})
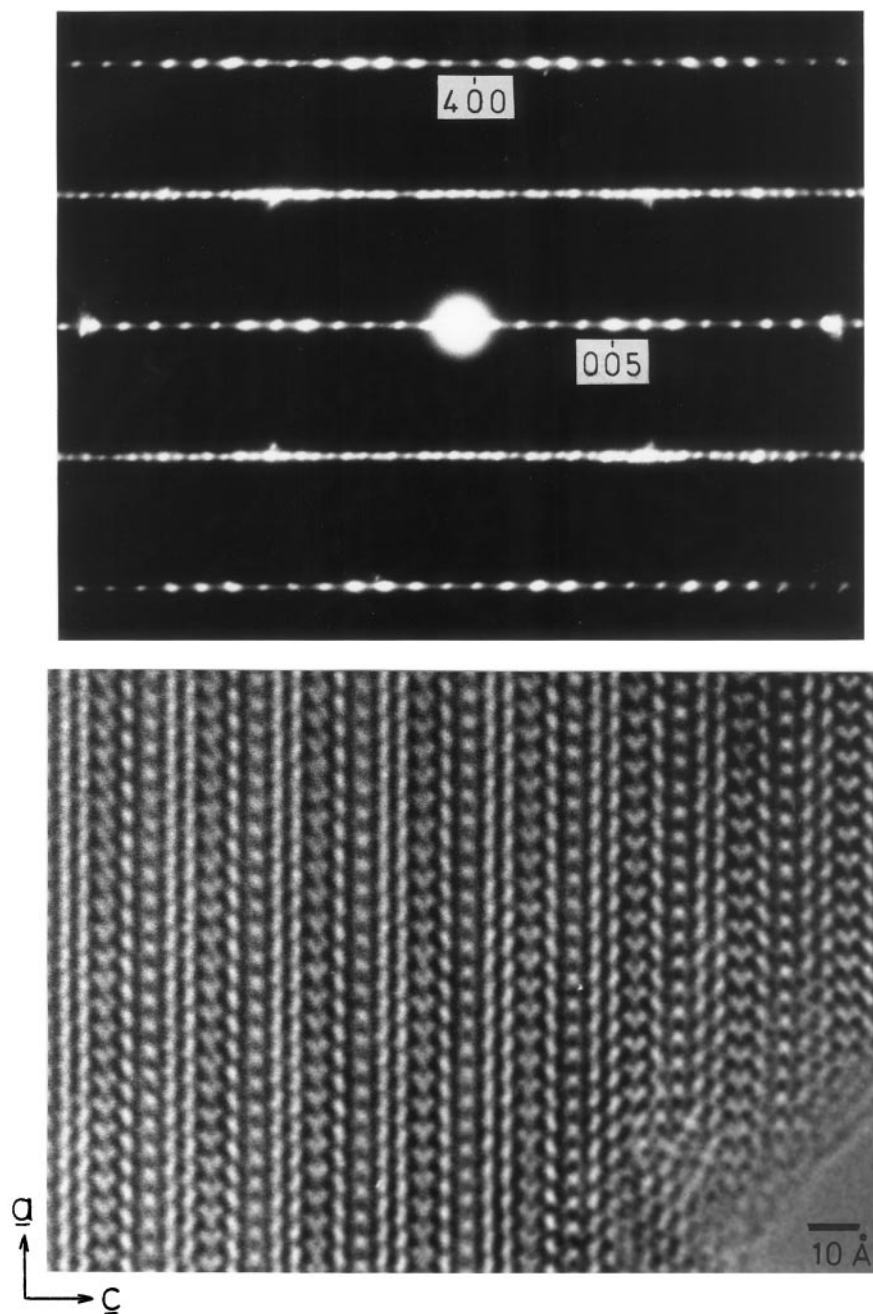
FIG. 3. Electron diffraction pattern, upper, and corresponding image, lower, for anosovite oxidized at 110°C. The scale bar on the image corresponds to 10 Å.

was used for these sites. The refinement converged at $R_{wp} = 0.13$ and $R_{bragg} = 0.07$. The refined unit cell parameters for the M_6O_{11} intergrowth were $a = 9.946(2)$, $b = 3.744(2)$, $c = 20.994(3)$ Å, and $\beta = 93.30(1)°$. The refined atomic coordinates are listed in Table 2. A plot showing the observed and calculated PXRD patterns from the Rietveld refinement is given in Fig. 8.

The refined structural parameters for the M_6O_{11} intergrowth phase were used in multislice image calculations in projection along the b axis. The image simulation is compared with the experimental image in Fig. 9. A good match of the main features and periodicity was obtained using a crystal thickness of 50 Å, a beam defocus of -450 Å, and a resolution of 2.5 Å. It was noted however that in the
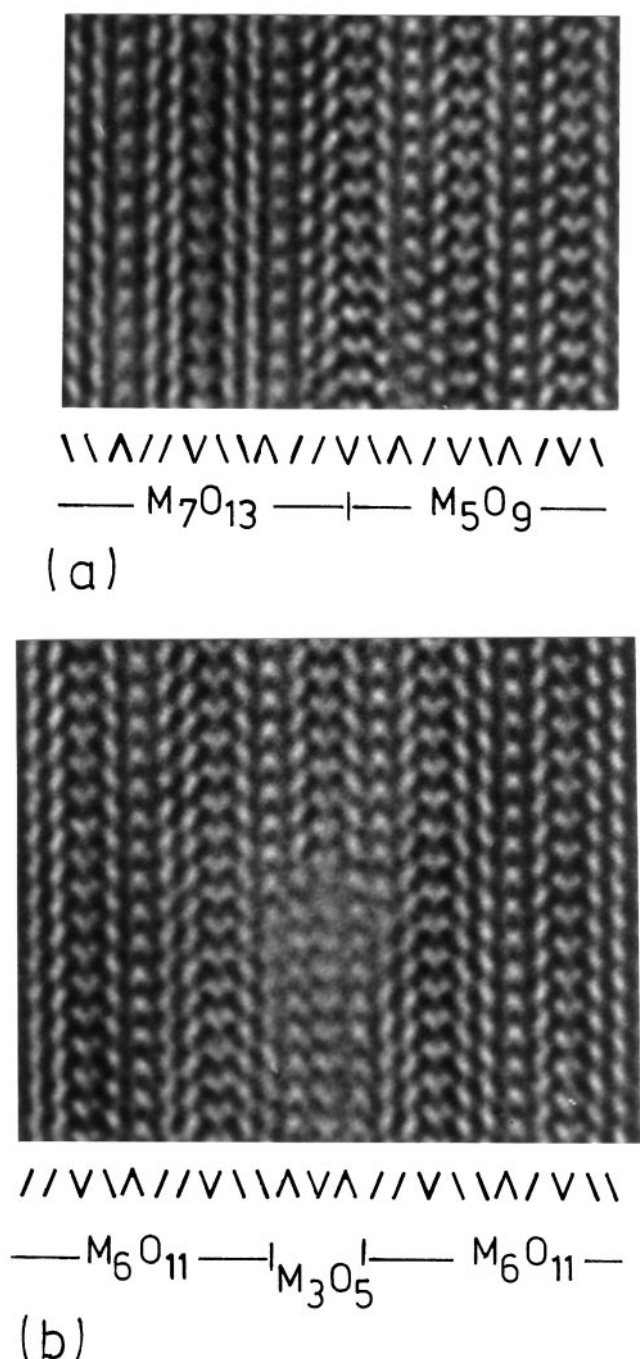
FIG. 4. High-resolution images from different regions of the low-temperature (110°C) oxidation product of anosovite.

lence in the experimental TEM image suggests that the space group may be Cm rather than $C2/m$, possibly due to ordering of magnesium in the M sites. Unambiguous justification for the noncentrosymmetric space group was not obtained because of refinement problems with the large number of variables and the poorly resolved PXRD patterns.

Discussion of Structures

A polyhedral representation of the M_6O_{11} structure is shown in Fig. 7. It comprises parallel slabs of anatase and M_3O_5 structures, with the orientation relations $(001)//(001)_{M_3O_5}//(101)_{an}$ and $[010]//[010]_{M_3O_5}//[010]_{an}$. The structure can alternatively be described in terms of unitcell twinning of anatase, with the twin plane as $(101)_{an}$ and with extra metal atoms occupying octahedral interstices within the twin planes. This description is emphasized in Fig. 7 by showing the anatase blocks in light shading and the octahedra in the twin planes in dark shading. The M_3O_5 structure of anosovite fits this description and is the first member of a series as previously noted in Ref. 9. It can be decomposed into pairs of $(101)_{an}$ octahedral sheets which individually have an MO_3 composition. These sheets connect by corner-linking of octahedra across the twin planes giving $M_2O_4O_{2/2} = M_2O_5$. Insertion of a metal atom in the twin planes gives M_3O_5. It is interesting to note that the same $(101)_{an}$ sheets occur in the mineral brannerite. In this case they are not interconnected but are held together by interlayer thorium atoms, giving the composition $Th(TiO_3)_2 = ThTi_2O_6$ (19).

The next members of the chemically twinned anatase series are M_5O_9 and M_7O_{13}, where the anatase layers are now 2- and 3-octahedra wide. Regions corresponding to these intergrowth phases are shown in Fig. 4a. The dominant phase in the low-temperature oxidized anosovites, M_6O_{11}, is actually an ordered intergrowth of elements of M_5O_9 and M_7O_{13}, so the anatase blocks are alternatively 2- and 3-octahedra wide as seen in Fig. 7. For the starting anosovite composition of $Mg_{0.3}Ti_{2.7}O_5$ the composition corresponding to full oxidation of the titanium is $MgTi_9O_{19}$. An ordered intergrowth of this composition would comprise twinned anatase blocks that are alternately 4- and 5-octahedra wide. Regular intergrowths with wider anatase blocks were not readily identified in the TEM images of more oxidized samples. As seen from Fig. 5, the TEM images of a sample oxidized at 400°C (phase B in Table 1) show complex irregular sequences of anatase and other structural elements. The ED patterns for this sample show small clusters of closely spaced spots which are incommensurate with the anatase subcell and the PXRD peaks are further broadened relative to those for the $\leq 300°C$ oxidtion products. Further analysis of the diffraction data for these more oxidized samples was not attempted.

experimental image the vee-shaped low-density regions are well defined but the inverted vee-shaped regions are not as clearly defined. In the M_6O_{11} structure the V and Λ regions are symmetry related (by the 2-fold axis in $C2/m$) and are thus equivalent in the image simulation. The lack of equiva-
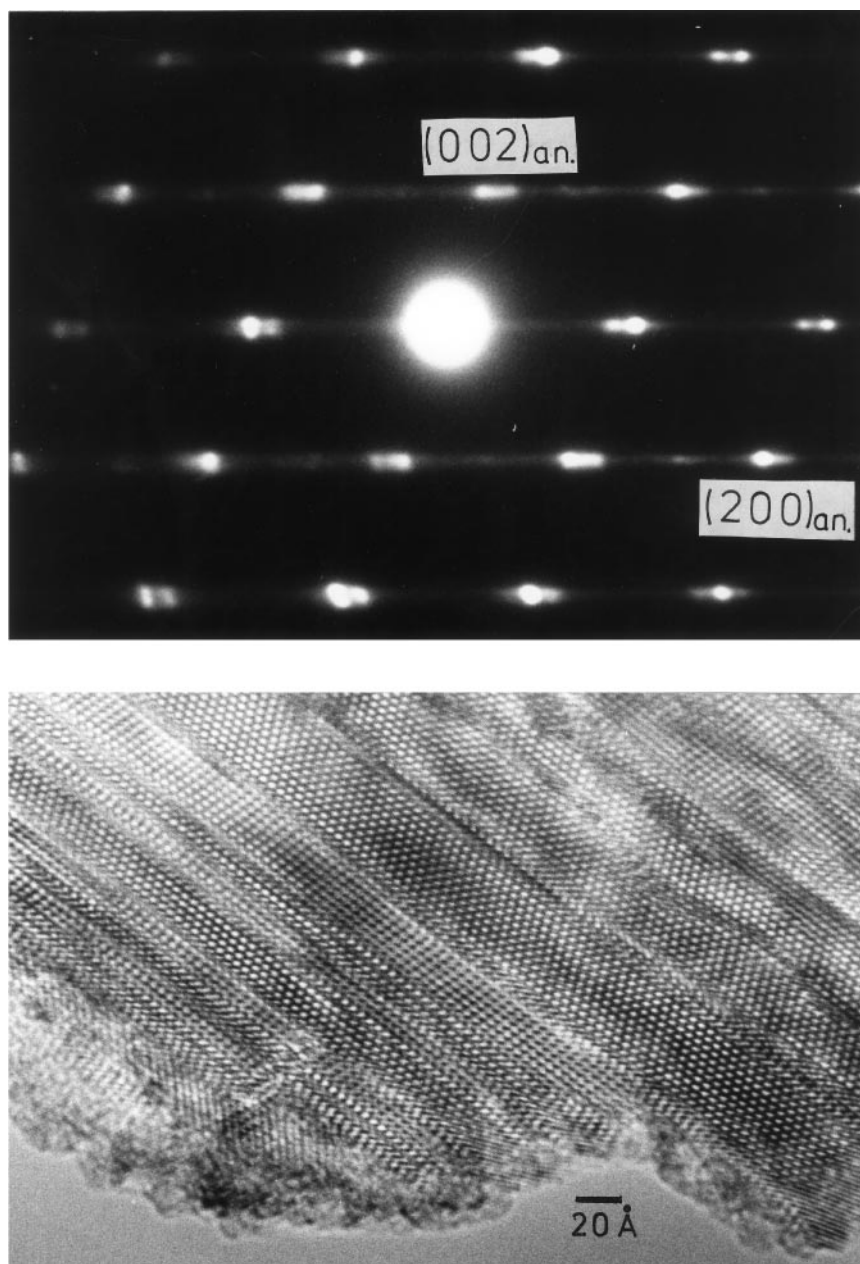
FIG. 5. Electron diffraction pattern, upper, and corresponding image, lower, for anosovite oxidized at 400°C. The scale bar on the image corresponds to 10 Å.

The M_3O_5 structure type, as exemplified by anosovite and pseudobrookite, Fe_2TiO_5, is unusual in that it can form coherent interfaces with a number of different structure types. In this paper the close structural match to anatase is emphasized. Structural coherence of M_3O_5 with the rhombohedral M_2O_3 structure type has also been demonstrated (20), for the case of epitaxial overgrowth of pseudobrookite with hematite. The orientation relations in this case are $(001)_{M_3O_5}//(001)_{M_2O_3}$ and $[110]_{M_3O_5}//\{110\}_{M_2O_3}$ (hexagonal indices for M_2O_3). In earlier studies we showed that low-temperature oxidation of Ti_3O_5 in H_2SO_4 leads to topotactic growth of the α-PbO_2 form of titania on its surface (6). In this case the orientation relations are $(110)_{Ti_3O_5}//(101)_{TiO_2}$ and $[001]_{Ti_3O_5}//[101]_{TiO_2}$. This topotactic growth of the high-pressure form of titania on Ti_3O_5 is remarkable because it was conducted at atmospheric pressure, whereas previous preparations required some tens of kilobars to stabilize the α-PbO_2 form relative to rutile.
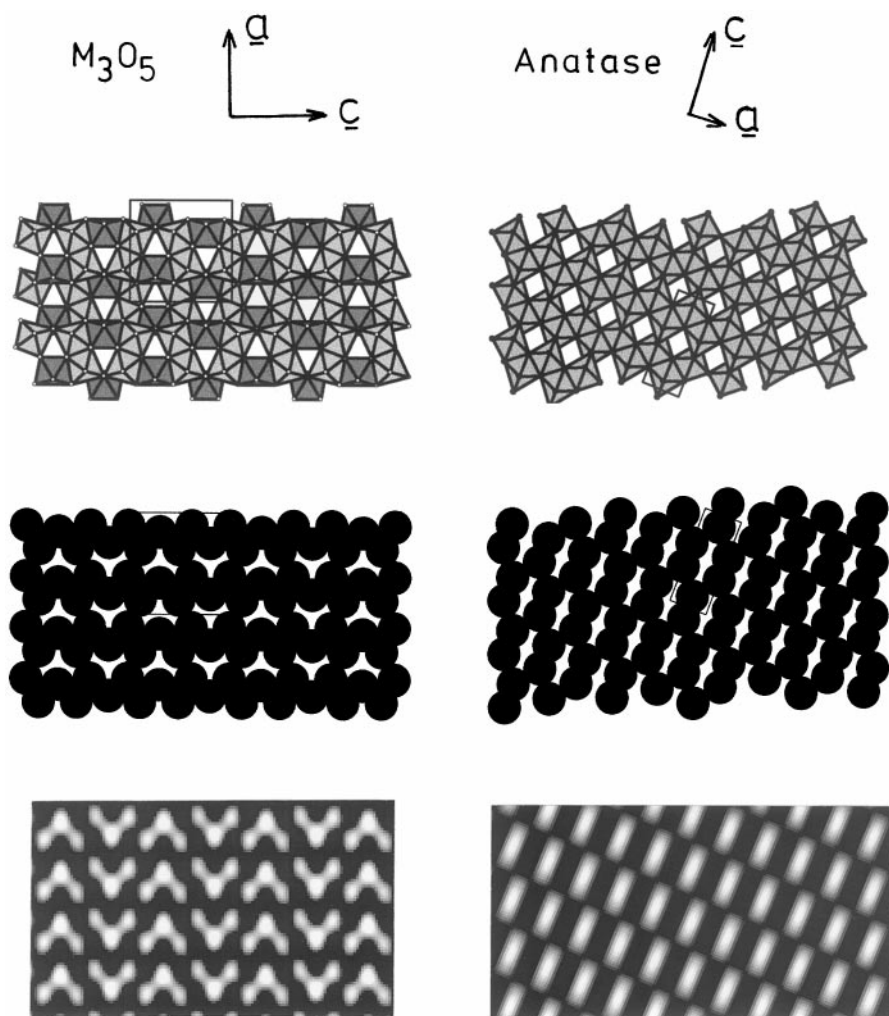
FIG. 6. Polyhedral representations of the anatase and M_3O_5 structures projected along their 3.8-Å axes (upper), together with projections of the metal atoms only (middle) and image simulations (lower).

CONCLUSIONS

This study illustrates the benefits of using the results from TEM studies in conjunction with powder XRD results to determine and refine the structures of phases formed under conditions where long-range ordering is not well developed. The oxidation is anosovite at $\leq 300°C$ was shown to result in the formation of a new phase for which structural homogeneity was restricted to regions of only 100–200 Å, due to the low driving force for ordering at these temperatures, and the heterogeneous nature of the oxidation which gave rise to microtwinning and other local atomic arrangements. The resulting PXRD patterns showed broad peaks (FWHM $\sim$ 0.7°) due to the lack of long-range order, which would have made structure analysis without the aid of TEM very difficult. The careful application of high-resolution TEM, using suitably thin crystals and defocus conditions, gave images that could be directly interpreted in terms of projected charge density, and which led directly to the establishment of a structural model which was then refined using the PXRD data.
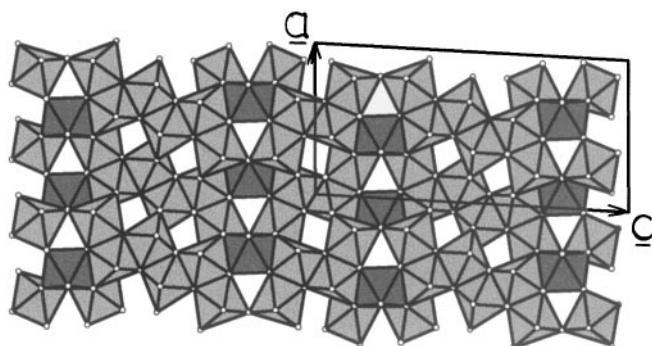

FIG. 7. Polyhedral model for M_6O_{11}, projected along [010]. Polyhedra associated with $M(1)$–$M(5)$ and $M(7)$ have light shading while polyhedra associated with $M(6)$ have dark shading to emphasize the twinned anatase regions.

TABLE 2

Atomic Coordinates from Rietveld Refinement for M_6O_{11}, Space Group $C2/m$, $R_{wp} = 0.13$, $R_{bragg} = 0.07$, $a = 9.946(2)$, $b = 3.744(2)$, $c = 20.994(3)$ Å, $\beta = 93.30(1)°$

Atom	x	y	z
$M(1)$	0.209(1)	0	0.1092(7)
$M(2)$	0.230(1)	0	0.2878(7)
$M(3)$	0.957(1)	0	0.3567(6)
$M(4)$	0.144(1)	0	0.4714(7)
$M(5)$	0.107(1)	0	0.7951(6)
$M(6)$	0.074(1)	0	0.9441(6)
$O(1)$	0.381(5)	0	0.054(2)
$O(2)$	0.115(4)	0	0.328(2)
$O(3)$	0.303(3)	0	0.211(2)
$O(4)$	0.030(4)	0	0.143(2)
$O(5)$	0.054(4)	0	0.273(2)
$O(6)$	0.436(5)	0	0.367(2)
$O(7)$	0.166(5)	0	0.386(2)
$O(8)$	0.334(4)	0	0.505(2)
$O(9)$	0.062(5)	0	0.558(2)
$O(10)$	0.204(5)	0	0.708(2)
$O(11)$	0.220(4)	0	0.873(2)

The structure of the low-temperature oxidation product can be described in terms of periodic unit cell twinning of two-dimensional $(101)_{an}$ anatase blocks that are alternately 2- and 3-octahedra wide. The composition of this twinned framework is M_5O_{11}. An extra metal atom per formula unit occupies octahedral sites in the twin planes, giving the composition M_6O_{11}. According to this description, the anosovite structure comprises single-octahedra-wide $(101)_{an}$ anatase layers with a third metal occupying the twin plane. Other members of this series with $(101)_{an}$ anatase blocks 2-octahedra wide (M_5O_9) and 3-octahedra wide (M_7O_{13}) were identified as minor components in local regions of the oxidised samples by TEM.

Sulfuric acid digestion tests were made on the products from the low-temperature oxidation tests, using the laboratory digestion apparatus previously described (8). These showed that the M_6O_{11} phase formed at $\leq 300°C$ remained fully soluble under simulated sulfate-plant digestion conditions. The solubility decreased when the oxidation temperature was increased above 300°C.
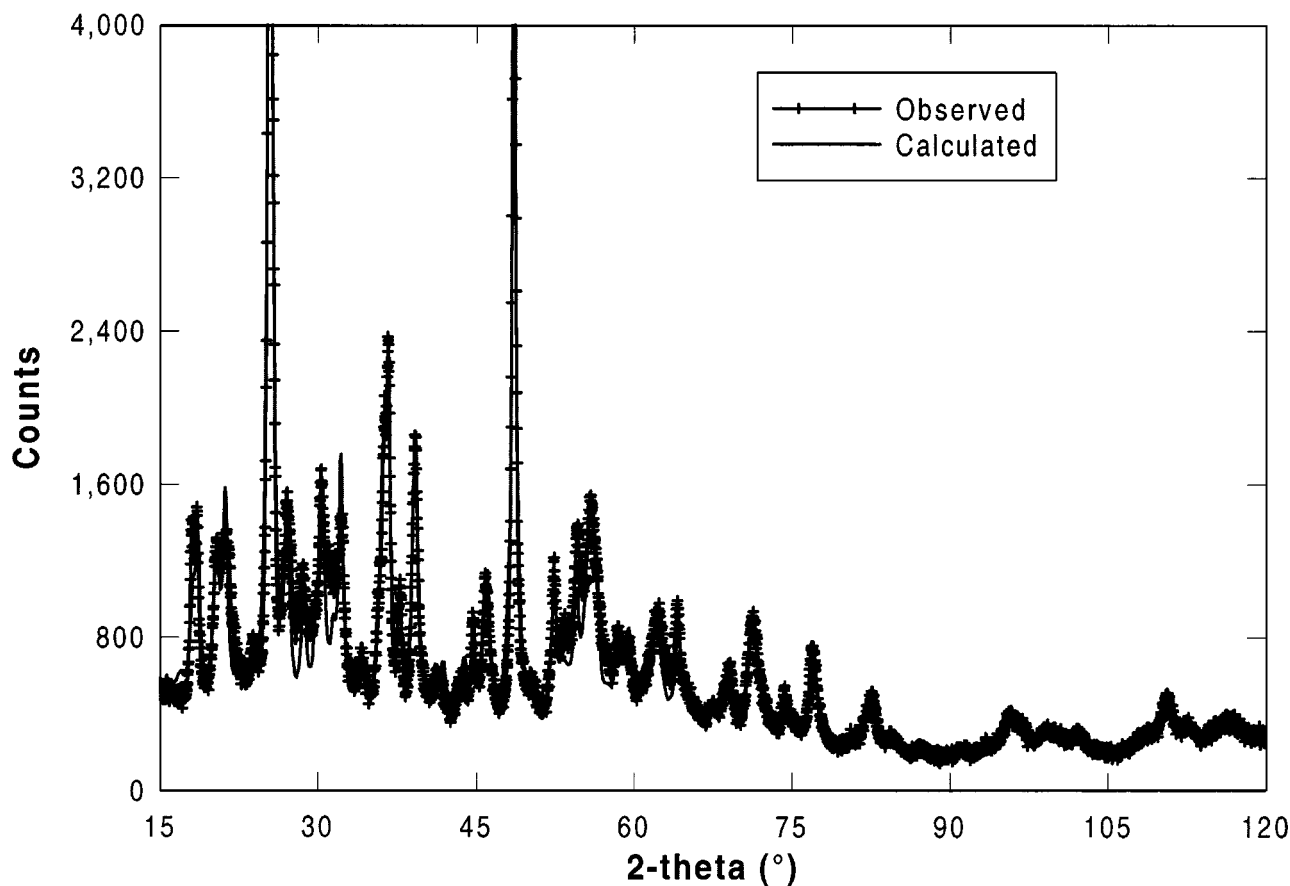

FIG. 8. Observed (crosses) and calculated (solid line) powder X-ray diffraction patterns from Rietveld refinement of the M_6O_{11} intergrowth phase.

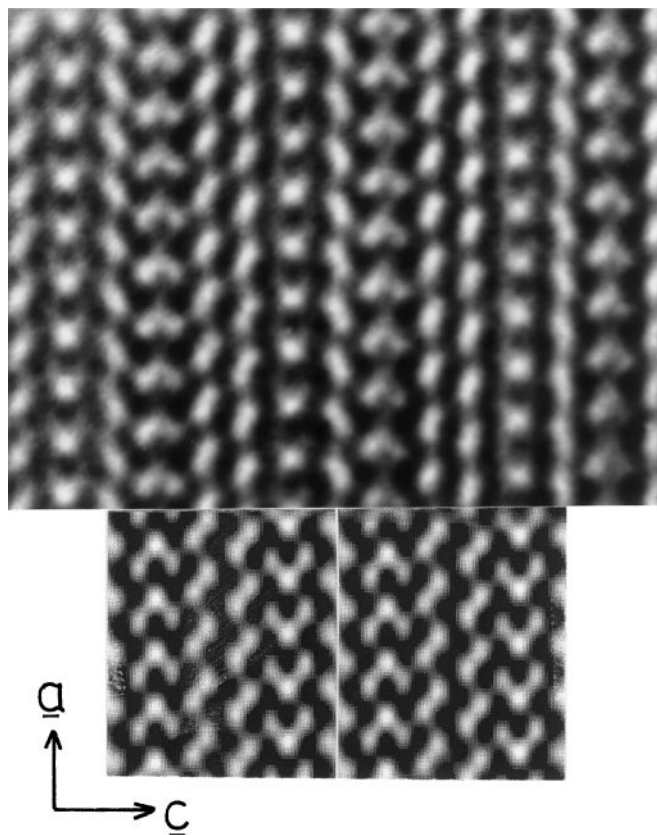**FIG. 9.** TEM image for M_6O_{11}, viewed along [010] (upper) together with image simulation (lower).

REFERENCES

1. J. Barksdale, "Titanium. Its Occurrence, Chemistry, and Technology," 2nd ed., Ronald Press, New York, 1966.
2. H. Y. Lee and D. Poggi, *Can. Metall. Q.* **17,** 93 (1978).
3. I. D. Martin and H. W. Hockin, U.S. Patent, 3,502,460, 1970.
4. I. E. Grey, C. Li, and I. C. Madsen, *J. Solid State Chem.* **113,** 62 (1994).
5. G. S. Zhdanov and A. V. Rusakov, *Tr. Inst. Kristallogr. Akad. Nauk. USSR* **9,** 165 (1954).
6. I. E. Grey, C. Li, I. C. Madsen, and G. Braunshausen, *Mater. Res. Bull.* **23,** 743 (1988).
7. I. E. Grey and R. Stranger, *J. Solid State Chem.* **101,** 331 (1992).
8. I. E. Grey, M. R. Lanyon, and R. Stranger, *Aust. J. Chem.* **49,** 801 (1996).
9. A. R. Landa-Canovas and L. C. Otero-Diaz, *Electron Microscopy 1998*, *Symp. GG* **111,** 305 (1998).
10. I. E. Grey, A. F. Reid, and D. G. Jones, *Inst. Mining Met. Trans., Sect. C* **83,** 105 (1974).
11. H. M. Rietveld, *J. Appl. Crystallogr.* **2,** 65 (1969).
12. R. J. Hill and C. J. Howard, *J. Appl. Crystallogr.* **18,** 173 (1985).
13. D. B. Wiles and R. A. Young, *J. Appl. Crystallogr.* **14,** 149 (1981).
14. G. Cagliotti, A. Paoletti, and F. P. Ricci, *Nucl. Instrum.* **3,** 223 (1958).
15. "International Tables for X-ray Crystallography," Vol. IV. Kynoch Press, Birmingham, U.K., 1974.
16. A. Coelho, "Topas Rietveld for Windows," Beta Test Version. Bruker AXS, 1999.
17. L. A. Bursill, J. L. Peng, and X. D. Fang, *Aust. J. Chem.* **45,** 1527 (1992).
18. C. J. Howard, T. M. Sabine, and F. Dickson, *Acta Crystallogr. Sect. B* **47,** 462 (1991).
19. A. D. Wadsley and R. Ruhr, *Acta Crystallogr. Sect. A* **21,** 974 (1966).
20. T. Armbruster, *N. Jb. Miner. Mh.* 109 (1979).